Dilution versus fractionation: Separation technologies hyphenated with spICP-MS for characterizing metallic nanoparticles in aerosols

Tianyu Cen [a,b], Yi-Bo Zhao [c,d], Andrea Testino [a,e], Jing Wang [c,d], Laura Torrent [a,*], Christian Ludwig [a,b,**]

[a] Laboratory for Sustainable Energy Carriers and Processes (LEP-CPM), Energy and Environment Research Division (ENE), Paul Scherrer Institut (PSI), CH-5232 Villigen PSI, Switzerland
[b] Environmental Engineering Institute (IIE, GR-LUD), School of Architecture, Civil and Environmental Engineering (ENAC), École Polytechnique Fédérale de Lausanne (EPFL), CH-1015 Lausanne, Switzerland
[c] Institute of Environmental Engineering, ETH Zürich, CH-8093 Zürich, Switzerland
[d] Laboratory for Advanced Analytical Technologies, EMPA, Swiss Federal Laboratories for Materials Science and Technology, CH-8600 Dübendorf, Switzerland
[e] STI SMX-GE, École Polytechnique Fédérale de Lausanne (EPFL), CH-1015 Lausanne, Switzerland

ARTICLE INFO

ABSTRACT

The presence of metal salts has become one of the major limitations for measuring metallic nanoparticles (NPs) in single particle inductively coupled plasma mass spectrometry (spICP-MS). Their presence generates a background signal in spICP-MS that can be overlapped with the signal intensity of small particles, leading to inaccurate NP size distributions. To overcome this analytical problem, sample pretreatment methods (e.g. dilution or fractionation) have been applied to liquid samples before spICP-MS measurements to minimize the ionic interference. However, the number of studies focused on reducing the presence of metal salts in aerosol characterization is limited. In this contribution, we investigated three different technologies coupled to an ICP-MS for online separating metallic NPs signals from ionic interference signals of metal salts in the aerosol. A rotating disk diluter (RDD) was used for the online dilution of the aerosol, while a differential mobility analyzer (DMA) and a centrifugal particle mass analyzer (CPMA) were used for the online fractionation of specific-sized NPs in the aerosol. The results from the analysis of 100 nm gold NPs (AuNPs) mixed with gold salts (Au^{3+}, mass ratio 1:25) showed the particle size limit of detection decreased from 78 nm to 61, 50, and 33 nm by using RDD, CPMA, and DMA respectively. In addition, it was found that the separation performance of AuNPs was in the order of DMA > RDD > CPMA. The methods used in this study based on spICP-MS have the potential to characterize directly NPs in complex aerosols containing metal salts.

1. Introduction

Airborne heavy metals have presented severe threats to the environment and human health (Mahowald et al., 2018). Except for natural processes like volcanic eruptions (Edmonds, Mason, & Hogg, 2022; Mason et al., 2021) and wildfire (Alves et al., 2011; Zauscher, Wang, Moore, Gaston, & Prather, 2013), human activities including mining (Csavina et al., 2012), fireworks (Moreno et al., 2010), combustion (Jahn et al., 2021), and e-cigarette (Zhao et al., 2020) contribute to emissions of heavy metals into the atmosphere and which also can be inhaled. Up to now, the characterization of airborne heavy metals from the atmospheric environment is still based on a "cocktail" effect analysis, where the contributions of metal salts, metal clusters, and metallic nanoparticles (NPs) could not be well separated from each other (Egorova & Ananikov, 2017; Haghani et al., 2020). The traditional aerosol metal characterization is based on offline filter collection followed by inductively coupled plasma (ICP) based analysis, which could be time-consuming. In addition, size information can be lost due to the digestion step before ICP analysis or deviated because of the secondary reactions on sample filters (Moreno et al., 2011; Yang et al., 2023). Therefore, in-situ and online methods for rapid measurement of aerosol metal have been developed to avoid the loss of the total amount of metals during collection, transportation, and storage. For example, with an extractive electrospray ionization time-of-flight mass spectrometer (EESI-TOF) the aerosol metal concentration could be obtained every second (Giannoukos et al., 2020, 2021). X-ray fluorescence spectrometry (XRF) allowed obtaining the elemental concentration of particulate matter (Furger et al., 2017, 2020). The electrochemical methods also provided metal aerosol concentration cost-effectively and rapidly (Mettakoonpitak, Volckens, & Henry, 2019; Zhao et al., 2023; Zhao et al., 2022). Nonetheless, the aforementioned online methods are not able to distinguish or analyze the different metal fractions (metallic NPs or metal salts) in an integrated manner.

In recent years, single particle inductively coupled plasma mass spectrometry (spICP-MS) has shown its potential for characterizing metallic NPs in liquid environmental samples (Bolea et al., 2021; Mozhayeva & Engelhard, 2020). This ICP-MS analysis mode is based on short dwell time measurements for sufficiently diluted samples, where the metallic NP signals appear as individual peaks in the acquired data. The frequency of the peaks represents the particle number concentration in the samples. The height or area of each peak (depending on the dwell time used) is directly correlated to the particle mass. The ionic background from the metal salt solution is presented as a stable signal, where the average intensity corresponds to the metal salt concentration in the solution. In addition, the presence of this ionic background can overlap with the metallic NPs signal, causing poor differentiation between metal salts and small metallic particles. To solve this problem, several strategies have been assessed in previous studies: (1) Decrease the dwell time in the ICP-MS detector (Strenge & Engelhard, 2016); (2) Offline dilution of the sample before the measurement (Schwertfeger, Velicogna, Jesmer, Scroggins, & Princz, 2016); (3) Offline separation of metallic NPs and metal salts before the measurement by using sample pretreatment methods such as cloud point extraction (CPE) (López-Mayan, Barciela-Alonso, Domínguez-González, Peña-Vázquez, & Bermejo-Barrera, 2020; Torrent, Laborda, Marguí, Hidalgo, & Iglesias, 2019; Wimmer et al., 2021) or magnetic ion adsorption (Luo et al., 2018); (4) Online separation based on hyphenation technologies like asymmetrical flow field-flow fractionation (AF4) (Hetzer, Burcza, Gräf, Walz, & Greiner, 2017; Meili-Borovinskaya et al., 2021), hollow fiber ultrafiltration (HFUF) (Jiang et al., 2023), hydrodynamic chromatography (HDC) (Pergantis, Jones-Lepp, & Heithmar, 2012), or ion-exchange column (IEC) (Hadioui, Peyrot, & Wilkinson, 2014, 2015); (5) Building up mathematical models for signal deconvolution (Cornelis & Hassellöv, 2013; Gundlach-Graham & Lancaster, 2022). Among the mentioned solutions, the decrease in dwell time relies on the detector hardware in the instrument. The mathematical model that is applied after the measurement depends on the quality of the data obtained and the accuracy of the model. Up to now, offline sample pretreatment or online hyphenation technologies are the common ways of reducing the amount of ionic interference from metal salt solutions in NPs characterization.

Up to now, spICP-MS has still not been widely applied for direct ambient aerosol characterization since most of the ICP-MS run with Ar as a carrier gas. However, even before the wide use of spICP-MS, some hyphenated technologies have been employed for aerosol characterization by ICP-MS. Scanning mobility particle sizer (SMPS) was coupled to ICP-MS to get the particle size distribution and the elemental composition simultaneously (Foppiano, Tarik, Gubler Müller, & Ludwig, 2018a; 2018b; Hess, Tarik, Losert, Ilari, & Ludwig, 2016; Tarik, Foppiano, Hess, & Ludwig, 2017). In this combination, the differential mobility analyzer (DMA) from the SMPS ran in scanning mode to select particles of different sizes according to their electrostatic mobility. The condensation particle counter (CPC) was connected to the ICP-MS in parallel. Therefore, the particle number concentration (CPC) and the elemental composition (ICP-MS) of different-sized NPs could be obtained simultaneously. In this work, only the average intensity of the target element contained in all particles of the same size (e.g., metallic nanoparticles, metal salts, metal oxides) was obtained because the ICP-MS analysis was not carried out in single particle mode. In addition to selecting particles at a given size, the DMA can also work as a gas converter. When using Ar as the sheath gas, DMA can convert the aerosol into "argonsol" for the NP characterization in ICP-MS (Myojo, Takaya, & Ono-Ogasawara, 2002). However, it also brings the limitation that the DMA cutoff size working in Ar is smaller than working in air because of the reduced breakdown voltage in Ar. In addition, gas exchange devices (GED) are also used as gas converters (Ohata, Sakurai, Nishiguchi, Utani, & Günther, 2015; Ohata & Nishiguchi, 2017). In a double-layer concentric glass tube, the sample flow passes through the inner channel and the Ar flow is in the outer channel, producing the gas matrix exchange through a diffusion process. With the development of spICP-MS analysis, the hyphenation of DMA-GED-spICP-MS has been employed as a two-dimensional setup for characterizing NPs aggregation states or NPs with different shapes (Tan et al., 2016, 2019). In spICP-MS analysis, the particle number concentration should be at an adequate level to get accurate results. To solve this problem in the aerosol, usually a rotating disk diluter (RDD) is used by adjusting the rotating speed to achieve the proper online dilution. For example, the hyphenation of DMA-RDD-spICP-MS was used for characterizing the aggregation state of AuNPs after sintering (Bierwirth, Olszok, Wollmann, & Weber, 2022). Up to now, the application of a hyphenated setup with spICP-MS in aerosol is still limited for characterizing pure metallic nanoparticles in presence of metal salts.

Recently, we have established a hyphenated system consisting of a rotating disk diluter (RDD) and an ICP-MS, which could run as an online sampling and dilution platform for metallic NPs characterization directly from the ambient aerosol (Cen, Torrent, Testino, & Ludwig, 2023a,b). By employing an external calibration strategy based on analyzing different-sized NP standards, the particle size distribution and the elemental composition could be obtained. However, it was observed that the presence of metal salts in the aerosol could have an effect on metallic NPs' characterization. In this case, traditional offline sample pretreatment methods could not be applied because the aerosol is always characterized online. Moreover, most of the online hyphenation technologies do not work either, since methodologies like AF4, HFUF, HDC, or IEC are only available for liquid samples. Therefore, online separation technologies for reducing ionic interference from metal salts need to be developed for the direct characterization of metallic NPs in the aerosol. In this study, gold (Au) was selected as the standard element because it is monoisotopic and Au nanoparticles (NPs) are stable engineered nanoparticles that will not get dissolved or oxidized in either liquid suspensions or in aerosol phase. Therefore, the mass ratio between AuNPs and gold salt (Au^{3+}) remains constant during evaluating different separation technologies in the aerosol including aerosol dilution and fractionation. For online dilution, an RDD was used by applying different dilution ratios (DRs) to decrease the ionic background level from metal salts. Therefore, the signal of metallic NPs in spICP-MS could be separated. For online fractionation, Differential Mobility Analyzer (DMA) and Centrifugal Particle Mass Analyzer (CPMA) were investigated to select a specific size range of metallic NPs that allowed reduction of ionic interference from metal salts in the aerosol for improving metallic NPs characterization in spICP-MS.

2. Experimental part

2.1. Chemicals

Gold nanoparticles (AuNPs) with different sizes (40, 60, 80, and 100 nm) stabilized in sodium citrate (2 mM) purchased from Nanocomposix (USA) were used as calibration standards. To generate metal salt particles in the aerosol, an ionic gold ICP standard (Sigma-Aldrich, USA) with an initial concentration of 1000 mg Au^{3+}/L was employed. Milli-Q water (18.2 MΩ cm, arium Pro VF Sartorius, Germany) was used to dilute both NP suspensions and metal salts solutions. Argon with 99.999% purity (PanGAS, Swiss) was used for all the ICP-MS measurements.

2.2. Setup description

The whole setup consists of functional sections including aerosol generation, aerosol fractionation or aerosol dilution, and aerosol characterization. For aerosol generation, a nebulizer originally from the commercial Agilent 7700× ICP-MS (Agilent Technologies, Japan) was employed as the introduction system. The sample was introduced by a peristaltic pump at 0.37 mL/min (0.1 rpm) and then a concentric nebulizer (Glass Expansion, Australia) created the wet aerosol using argon as the carrier gas. For liquid sample analysis (liquid mode), the wet aerosol generated from the nebulizer system is directly sent to the plasma by employing argon as carrier gas. However, in the proposed setup (aerosol mode), some adaptions were made to achieve online ionic interference reduction for characterizing NPs in aerosol samples (Fig. 1). The wet aerosol was first dried in a silica dryer to remove water vapor during the aerosol transport and avoid size deviation during the particle fractionation. For aerosol fractionation, a DMA or a CPMA was used for fractionating NPs at different sizes. For aerosol dilution, RDD was used by adjusting the rotating speed (from 10% to 100% with 10 cavities disk) to reach different dilution ratios (DR, nominally from 0.0067 to 0.067). Compared to liquid sample analysis, during aerosol transport, there can be pressure drops [37], which decrease the flow rate and further influence the aerosol characterization. To solve this problem, a vacuum pump was added after the RDD to maintain the sample flow rate at 0.9 L/min. Finally, at the outlet of the RDD, 0.9 L/min of argon controlled by an MFC brought the diluted sample into the ICP-MS for single particle analysis. A mixture of Xe/Ar
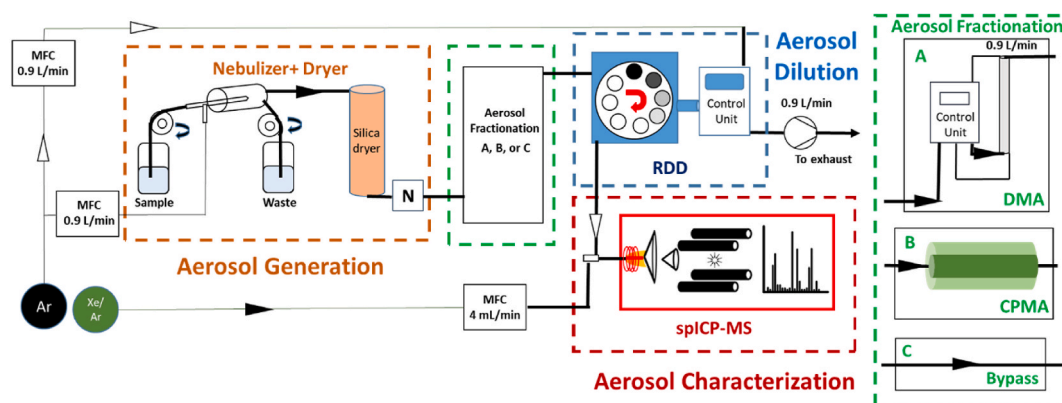

Fig. 1. Schematic representation of the proposed method for separating the signal of metal salts (Au^{3+}) and metallic nanoparticles (AuNPs). Options including (A) DMA, (B) CPMA could be chosen for aerosol fractionation, or (C) bypass.

(100 mg/mL Xe) at 4 mL/min was employed as the tuning gas by monitoring the [124]Xe sensitivity. The different gas flow rates were checked every day by using a primary flow calibrator (Gilibrator 2, Gillwaian, USA). The ICP-MS measuring parameters are summarized in Table S1 of the Supporting Information.

2.3. Setup calibration

In spICP-MS, usually, two calibration methods are feasible: 1) by using well-characterized NP standards of known sizes (Olesik & Gray, 2012), or 2) by using ionic standards with the determined transport efficiency from liquid to aerosol (Pace et al., 2011). In a previous study of RDD-spICP-MS working in aerosol mode, we used the NP standards approach since the transport efficiency of the system was unknown (Cen et al., 2023a,b). However, this method left the limitation that the commercial standard NPs are not available for all the elements. In addition, in a previous study, researchers reported the difference in transport efficiency from liquid to aerosol between metal salt solution and nanoparticles (i.e. ionic Pt > PtNPs) (Torregrosa, Grindlay, Mora, & Gras, 2023). This could affect the mass ratio between Au^{3+} and AuNPs when working in aerosol mode. Therefore, in this project, we did the calibration with the transport efficiency method.

To generate the aerosol with known transport efficiency, a concentric nebulizer was used as an introduction system in this project (Fig. 1, Aerosol Generation). In addition, a vacuum pump was put after the RDD to overcome the pressure drop during the aerosol transport. For comparison purposes, the transport efficiency in liquid mode (η_{lid}) was first evaluated with standalone ICP-MS working in single particle mode (without hyphenation). Then, the nebulizer and the dryer were combined with RDD-spICP-MS (Fig. 1, Bypass) to obtain the transport efficiency in aerosol mode (η_{aer}) using the same ICP-MS operating parameters (Table S1).

As it is explained in previous literature (Pace et al., 2011), there are three common methods including waste, size, and frequency for obtaining the η. In this case, the size and the frequency methods were used to calculate the η for AuNPs and Au^{3+}. The adapted formulas for the developed setup are shown in Table 1. To obtain the η of different sized particles by using the frequency method, 40, 60, 80, and 100 nm AuNP suspensions were diluted with Milli-Q water up to 10^6 #/mL. For each sized NPs, the peak intensity and the frequency were obtained from the time-resolved plot at each RDD DR. The DR at each position of the RDD was calibrated with NaCl based on a previous study (Cen et al., 2023a,b). Then, the same measurement was carried out for Au^{3+} using the standard solution, getting the average intensity for obtaining the η by the size method.

2.4. RDD online dilution for signal separation

To investigate the effect of online aerosol dilution on NP signal separation from the ionic background, RDD was coupled to an ICP-MS working in single particle mode (Fig. 1, Bypass). AuNP suspensions of 40 and 100 nm were prepared at 10^6 #/mL. Then, the Au^{3+} standard was diluted at different mass concentrations with Milli-Q water and mixed with the AuNP suspensions. For both 40 and 100 nm AuNPs, the mixture suspensions were prepared at a mass concentration ratios (Au^{3+}/AuNP) of 0 (only AuNPs without Au^{3+}), 1, 5, 10, and 25. For each mixture, the measurement was carried out at three RDD DRs (nominally at 0.02, 0.04, and 0.06). In addition, to compare the different behavior of ionic interference in aerosol and liquid mode, the same experiments were executed for liquid samples with the standalone ICP-MS working in single particle mode (without RDD). To fulfill the concentration range of spICP-MS analysis, both 40 and 100 nm AuNPs were prepared at $2 \cdot 10^7$ #/mL. The same mixture ratio of Au^{3+}/AuNP (0, 1, 5, 10, and 25) were used to investigate the ionic interference in liquid mode.

For the data treatment, an iterative algorithm based on μ+5σ was applied to obtain the threshold. This threshold is used for separating the NP signal from the ionic signal using a homemade MATLAB script (Cen, Torrent, Testino, & Ludwig, 2023a,b). The signal above the threshold can be regarded as the AuNPs, while the signal below the threshold belongs to Au^{3+}. After subtracting the average Au^{3+} intensity for each AuNP, the AuNP intensity is transferred to particle mass based on the determined η and then the size is calculated using bulk density and assuming a spherical shape. The particle size limit of detection (LOD_{size}) was obtained by using Equation (1) assuming a spherical shape of the particles. LOD_{size} [nm] is the equivalent particle size of the threshold intensity determined using the iterative algorithm aforementioned (Laborda, Gimenez-Ingalaturre, Bolea, & Castillo, 2020-a).

Table 1
Equations for obtaining the transport efficiency of liquid and aerosol samples.

	Frequency method	Size method
Liquid sample	$\eta_{lid} = \dfrac{N_{ICP}}{q_{liq} \times N_{liq}}$	$\eta_{lid} = \dfrac{k_{ion}}{k_p}$
Aerosol sample	$\eta_{aer} = \dfrac{N_{ICP}}{DR \times q_{liq} \times N_{liq}}$	$\eta_{aer} = \dfrac{k_{ion}}{k_p}$

N_{ICP} is the particle number obtained in spICP-MS per unit time (#/min), q_{liq} is the liquid sample flow rate (mL/min), N_{liq} is the particle number concentration in the liquid sample (#/min), DR is the RDD dilution ratio, k_p is the slope of the NP calibration curve obtained from the particle intensity versus the NP mass, k_{ion} is the slope of metal salts calibration curve obtained from the average ionic intensity versus the mass concentration.

$$LOD_{Size} = \left(\frac{6(Th - \mu)}{\rho \pi S} \right)^{\frac{1}{3}}$$

(1)

where *Th* is the threshold obtained from the iterative algorithm based on μ+5σ, *μ* is the average intensity of the ionic signal, *ρ* is the density of the particle, and *S* is the slope of the calibration curve between peak intensity and particle mass.

2.5. DMA online fractionation for signal separation

To investigate the effect of online fractionation on NP signal separation from the ionic background, a DMA was incorporated into the coupled setup. The DMA selected the particles present in the aerosol according to their electrical mobility. When the particle reached the balance between the drag force and the electric force, the particle's electrical mobility size (d_m) could be obtained from the DMA based on Equation (2) (Tan et al., 2016).

$$Z_p = \frac{neC_c(d_m)}{3\pi\mu d_m}$$

(2)

where Z_p represents the electrical mobility, d_m is the electrical mobility size, n is the number of charges on each particle, e is the elemental electrical charge, C_c is the Cunningham slip factor, which is influenced by d_m, and μ is the gas viscosity.

Usually, DMA is used for air-based aerosol measurements. In this case, the setup was running in argon mode, therefore a correction factor was applied due to the change of viscosity from air to argon, which would further influence the Z_p. Therefore, the mobility size with DMA working in argon mode was corrected by using certified sized polystyrene latex spheres. In addition, a scanning mobility particle sizer (SMPS) was coupled after DMA to evaluate the resolution of the DMA (Fig. S1). In this case, a 0.1% NaCl solution was prepared as the aerosol source. DMA was used to select the particle size from 40 to 100 nm with a step size of 10 nm. SMPS was used to obtain the particle size distribution after the fractionation of DMA. After the resolution evaluation, DMA was coupled to RDD-spICP-MS (Fig. 1) for the size fractionation analysis. A mixture of Au^{3+} and AuNPs (40 and 100 nm, respectively) at the mass concentration ratio of 25 was prepared, which was equivalent to the highest ratio tested in the online dilution experiment. The RDD with a disk of 10 cavities was fixed at DR of 0.06 to achieve the equivalent highest concentration as in the online dilution experiment. A scanning program was set for obtaining the signal at each size position. The gas flow rates in the DMA were set at 9 L/min for the sheath gas and at 0.9 L/min for the sample to maintain the ratio of 10:1 during the particle size selection. For the mixture containing 100 nm AuNPs, the scanning program started from 80 nm up to 120 nm with a step size of 2 nm. For each step, the spICP-MS measurement was carried out for 2 min. At each step change, the spICP-MS waited 1 min after changing the particle size to stabilize the signal. The same program was employed for the mixture containing 40 nm AuNPs, but the size range was set from 30 to 60 nm.

2.6. CPMA online fractionation for signal separation

CPMA was also evaluated as an online fractionation technology for NP signal separation from metal salts signal. In this case, the particle mass was directly selected based on the balance of electrostatic force and centrifuge force between two rotating electrodes (Johnson, Symonds, & Olfert, 2013; Olfert, Reavell, Rushton, & Collings, 2006). Equation (3) describes the CPMA fractionation.

$$m = \frac{neV_c}{\omega_c^2 r_c^2 \ln\left(\frac{r_2}{r_1}\right)}$$

(3)

where *m* is the mass of the selected particle that could pass through the CMPA, n is the number of charges on each particle, e is the elemental electrical charge, V_c, ω_c, and r_c are the voltage, angular velocity, and radius at the center between the two electrodes, r_2 and r_1 represent the two electrodes' radius.

Similar to the DMA, a coupled CPMA-SMPS system was used to evaluate the resolution of the CPMA (Fig. S1). The same 0.1% NaCl
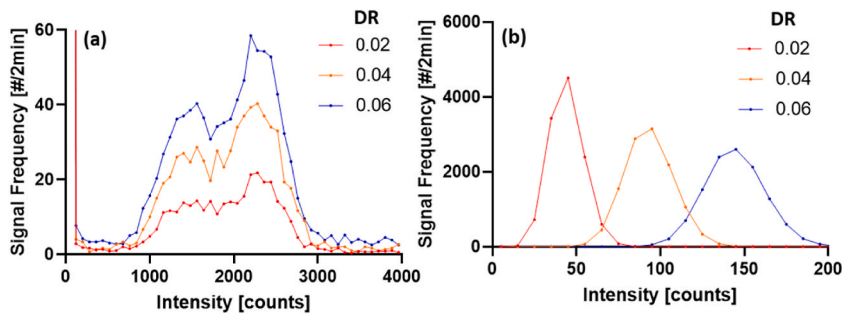

Fig. 2. The signal frequency of 100 nm AuNPs (a), and Au^{3+} at the equivalent mass concentration (b, 10 μg/L) for different DRs (0.02, 0.04, and 0.06) obtained by RDD-spICP-MS.

solution was used as the aerosol source. With the known density, the particle sizes were selected from 40 to 100 nm with a step size of 10 nm. After the resolution evaluation, the fractionation experiment was performed with AuNPs mixed with Au^{3+} by coupling CPMA to RDD-spICP-MS. The 10 cavities RDD disk was used and set at DR of 0.06 as well. For the 100 nm AuNPs mixed with Au^{3+}, the scanning program started from 80 nm up to 120 nm with a step size of 2 nm. For each step, the spICP-MS measurement was carried out for 2 min. At each step change, the spICP-MS waited 1 min after changing the particle size to stabilize the signal. The same program was employed for 40 nm AuNPs mixed with Au^{3+}, but the size range was set from 30 to 60 nm.

3. Results and discussion

3.1. Transport efficiency

To obtain the transport efficiency of the chemical species of interest in RDD-spICP-MS setup, AuNPs suspensions, and Au^{3+} solutions were measured in single particle mode at different DRs. As is shown in Fig. 2a, the signal frequency of 100 nm AuNPs was well separated from the background. When decreasing the nominal DR from 0.06 to 0.02, the particle frequency decreased accordingly but the intensity distribution remained constant. The same trend was found for other sized (40, 60, and 80 nm) AuNPs as shown in Fig. S2, which indicated that single particle intensity will not be affected during the online dilution process. Compared to 40 and 60 nm AuNPs, a bimodal intensity distribution was presented for 80 and 100 nm AuNPs (Fig. 2a and Fig. S2c). This effect was confirmed by the TEM results from the manufacturer certificate, where the bimodal distribution could be also observed. After the test with AuNPs, the same experiment was repeated for 10 μg/L Au^{3+}, which was at the same mass concentration of 100 nm AuNP (Fig. 2b). When decreasing the nominal DR from 0.06 to 0.02, unlike AuNP samples, the Au^{3+} intensity decreased as well. This effect was further confirmed with Au^{3+} samples at other mass concentrations from 0.5 to 50 μg/L (Fig. S3). The different behavior of AuNPs and Au^{3+} peak intensity in spICP-MS comes from the different effects of the online dilution. For AuNPs, when measured in single particle mode, each particle reaches the detector individually. Therefore, whatever the dilution is, the peak intensity is always proportional to the single particle mass, and the dilution only influences the frequency of the NPs reaching the detector. The particle number of Au^{3+} generated from the salt solution was far more than AuNPs. Hence, for each reading of the detector, the peak intensity was proportional to the amount of Au^{3+}. When applying the dilution, the peak intensity decreased due to the amount of Au^{3+} is reduced in the aerosol after the RDD.

After the RDD calibration, each RDD rotating speed could be converted into a specific DR. As shown in Fig. 3a, the particle frequency for each sized AuNPs follows a linear relationship with the DR. The slope of the curve is the parameter of N_{ICP}/DR. This parameter was used for determining the transport efficiency in aerosol mode by the particle frequency method (Fig. 3e). In addition, the calibration curve based on the peak intensity and the mass obtained from different-sized AuNPs and Au^{3+} (Fig. 3b) could be
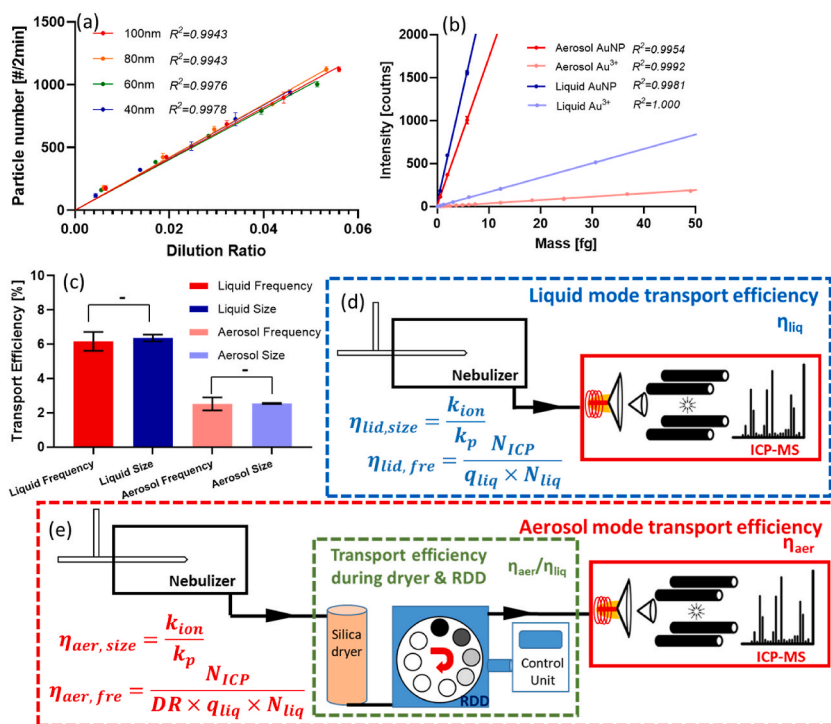

Fig. 3. Results from transport efficiency determination in liquid and aerosol mode via particle size and frequency methods. **(a)** Relationship between different sized AuNPs frequency (N_{ICP}) at different DR. **(b)** Relationship between intensity and AuNPs (k_p) or Au^{3+} (k_{ion}) mass. **(c)** Transport efficiency in liquid and aerosol mode via particle frequency and size methods. **(d–e)** Schemes of the setup running in liquid mode and aerosol mode.

obtained. As shown in Fig. 3b, both AuNPs (dark red) and Au^{3+} (light red) followed the linearity in the aerosol. The slopes referred to as k_p and k_{ion} were used for determining the transport efficiency in aerosol mode via the particle size method (Fig. 3e).

As a comparison, the same experiment was repeated in liquid mode with different-sized AuNPs at $2 \cdot 10^4$ #/mL and Au^{3+} at equivalent mass concentration. As it is shown in Fig. 3b, the sensitivity was higher in liquid mode (blue) than in aerosol mode (red). With the obtained slope and NP frequency, the transport efficiency with both calculation methods (size and frequency) could be obtained. As can be seen in Fig. 3c, no statistical differences were found between the transport efficiencies calculated from the frequency and size methods for both working modes (ANOVA test, p > 0.05). This fact indicated that the transport efficiency was the same for both AuNPs and Au^{3+} since the frequency method only relies on the number of AuNPs counted, meanwhile, the size method depends on the slope ratio between the calibration curves of AuNPs and Au^{3+}. However, the transport efficiency in aerosol mode was lower (around 2.5%) compared to liquid mode (6%). This difference may be mainly attributed to the diffusion and sedimentation loss effect during the aerosol transport. In liquid mode (Fig. 3d), the aerosol generated from the nebulizer is directly carried to the plasma. However, in aerosol mode (Fig. 3e), the generated aerosol passes through a longer path including the dryer and the online dilution system, which may cause more loss during the transport.

3.2. RDD online dilution for signal separation

Based on the previous experiment of pure AuNPs and Au^{3+} analysis (Fig. 2 and Fig. S2), we concluded that the online dilution in the RDD-spICP-MS system does not change the peak intensity of AuNPs, but it decreases the intensity of Au^{3+}. In this section, RDD was evaluated for separating the signals of the different gold forms present in the sample mixtures.

As shown in Fig. 4a and **4b**, in aerosol mode, both sensitivity levels for Au^{3+} and AuNPs were lower than the ones in liquid mode, which was the same effect we saw during the transport efficiency determination (Fig. 3b). In addition, unlike AuNPs, the behavior of Au^{3+} in aerosol mode is different from liquid mode. In aerosol mode, the standard deviation of the average intensity is almost double compared to liquid mode (Fig. 4d). A scheme in Fig. 4c is represented to explain the different behavior of AuNPs and/or Au^{3+} in liquid mode and aerosol mode. In the liquid mode, AuNPs were present as individual particles, while Au^{3+} was completely dissolved and homogenously distributed in the wet droplet. The generated wet droplets then were carried by an argon stream to the plasma, the mass analyzer, and the detector. The resulting Au^{3+} signal was represented as a stable baseline and each AuNP signal was represented as an individual peak (liquid mode). However, in aerosol mode, the fine wet droplets generated by the nebulization system passed through a silica dryer, which removed the water content, and consequently, each droplet formed dry aerosol. The size of AuNPs would remain the same as it was in the wet droplet. In the case of Au^{3+}, the metal salt particle size depends on the Au^{3+} mass in each droplet, which is related to the initial metal salt concentration in the liquid and the size of the droplet formed. Compared to AuNPs, the sensitivity of Au^{3+} particles was much lower due to the less presence of Au, where these particles also contain anions, and the lower density of those particles. In addition, the particles of Au^{3+} after the dryer were of various sizes and the number of small particles was far more than AuNPs.
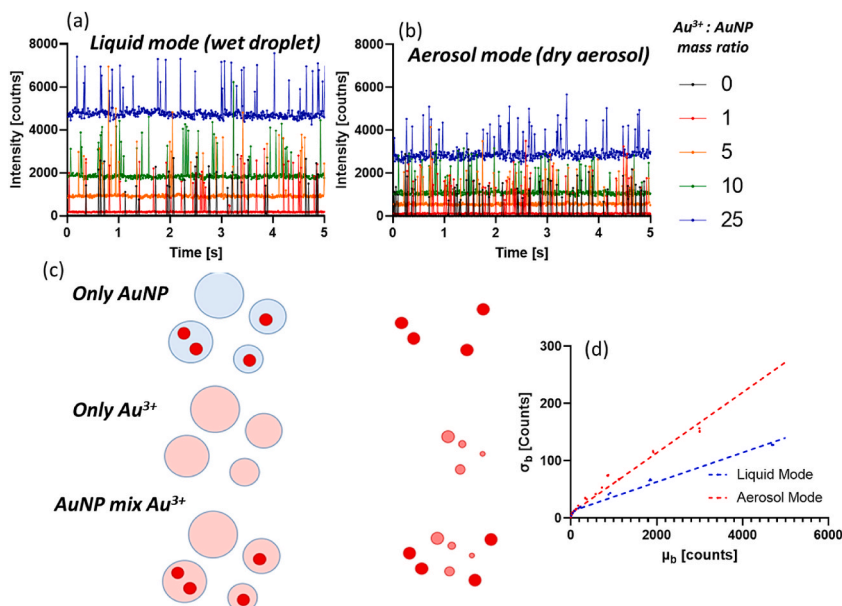
Fig. 4. Time-resolved plots of Au^{3+} mixed with 100 nm AuNPs at different mass ratios obtained from **(a)** spICP-MS analysis in liquid mode and from **(b)** RDD-spICP-MS analysis in aerosol mode. **(c)** Scheme of AuNPs and/or Au^{3+} aerosol formation during the aerosol generation and their transport. **(d)** Standard deviation (σ_b) at each average intensity (μ_b) of Au^{3+} analyzed in liquid (blue) and aerosol (red) mode. (For interpretation of the references to colour in this figure legend, the reader is referred to the Web version of this article.)

After subtracting the ionic signal based on an iterative algorithm of $\mu+5\sigma$, the time-resolved plot was transferred into histograms and finally presented as particle size distributions. As can be seen in Fig. S4, in liquid mode, the particle size distributions of 100 nm AuNPs remain constant at different Au^{3+} concentrations. With the increasing Au^{3+} concentration, the LOD_{size} increased as well, causing the loss of some signals at smaller particle size regions (smaller than the dashed line in Fig. S4). The same effect was observed for 40 nm AuNP mixture experiments (Fig. S5), where more particles were lost at higher Au^{3+} mix ratios as a consequence of the overlapping of the NPs and ionic signals.

The same experiments were performed in aerosol mode at different RDD rotation speeds (Fig. 5). The trend of LOD_{size} was similar to the liquid mode, where it increased with the Au^{3+} concentration. As can be observed in Fig. 5, working at DR (nominal 0.06), the particle number of 100 nm AuNPs decreased when increasing the Au^{3+} concentration with respect to the liquid mode. Compared to the 100 nm AuNP mixture sample, the particle number was less affected by the increase of Au^{3+} mixed with 40 nm AuNPs because of the relatively lower Au^{3+} concentration (Fig. S6). These results indicated that at the same mixture ratio, Au^{3+} would cause more interference for AuNP characterization in aerosol mode than in liquid mode.

Generally, the effect of ionic interference could come from the high background intensity and its large variation. To further understand each effect and the function of RDD online dilution, the ratio of particle intensity (I_p) to average of ionic background intensity (μ_b, Fig. 6a) was calculated for each sample working at a mass ratio of 1:25. The ratio of particle intensity (I_p) to standard deviation of the background intensity (σ_b, Fig. 6b) was investigated as well. For both 40 and 100 nm AuNPs, the I_p/μ_b in liquid mode was at a similar level to the one in aerosol mode if the nominal DR was at 0.06. However, I_p/σ_b was much smaller for aerosol mode, indicating more standard deviation of background intensity in aerosol mode. This may come from the different behavior of Au^{3+} in aerosol mode. As explained in Fig. 4, compared to liquid mode, the Au^{3+} in aerosol mode would form salt particles after the dryer and reach the ICP detector discontinuously.

In aerosol mode, for both 40 and 100 nm AuNPs mixed with Au^{3+}, online dilution via RDD could effectively decrease the interference from the average and the standard deviation ionic background (from DR at 0.06 to 0.02). The difference between 40 and 100 nm AuNPs, it is that at each DR, I_p/μ_b was much higher for 40 nm AuNPs, while I_p/σ_b was much higher for 100 nm AuNPs. This indicates that for smaller sized NPs, the ionic interference mainly came from the average intensity of the ionic species. For larger-sized NPs, the ionic interference rather originated from the standard deviation of the ionic background.

The improvement of NP separation from ionic background by RDD online dilution is also indicated by the particle number concentration (PNC, Fig. 6c and d) obtained from Equation S1. By decreasing the nominal DR from 0.06 to 0.02, the PNC of 100 nm AuNPs from the mixture ($AuNP/Au^{3+}$) detected by spICP-MS in the aerosol increased from 65% to 77% respect to pure AuNPs (Fig. 6c). For 40 nm AuNPs, when the nominal DR decreased from 0.06 to 0.02, the PNC of 40 nm AuNPs separated from the mixture ($AuNP/Au^{3+}$) increased from 87% to 102% respect to pure AuNPs (Fig. 6d). These results indicated RDD online dilution could help in the separation of NPs intensity from ionic signal by decreasing the average of ionic background (μ_b) and the standard deviation intensity (σ_b).

3.3. Online fractionation for signal separation

To improve the separation of AuNPs signal from ionic background in the presence of high amounts of Au^{3+}, DMA, and CPMA were
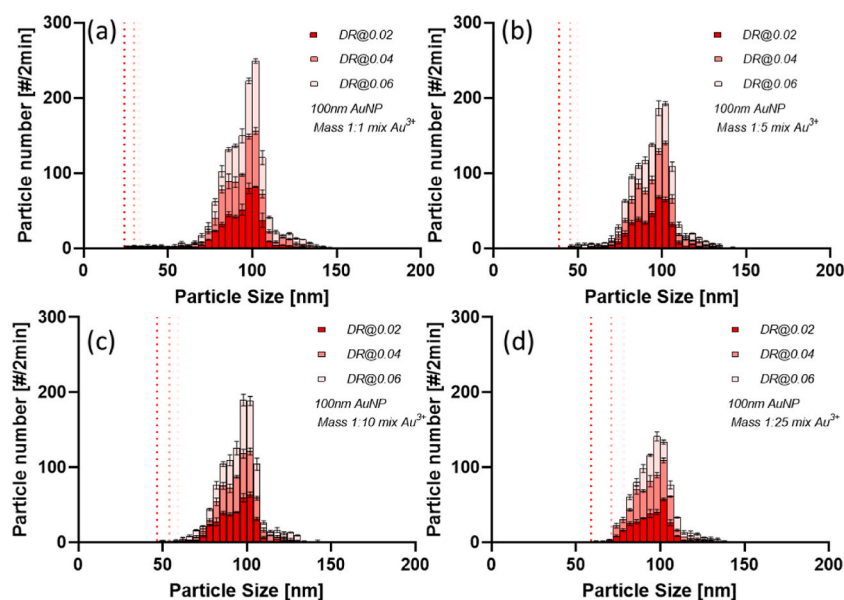

Fig. 5. Particle size distributions of 100 nm AuNPs mixed with Au^{3+} at different mass concentration ratios: 1:1 (a), 1:5 (b), 1:10 (c), and 1:25 (d) at different RDD DR (nominally 0.02, 0.04, and 0.06) in aerosol mode. The dash lines represent the LOD_{size}.
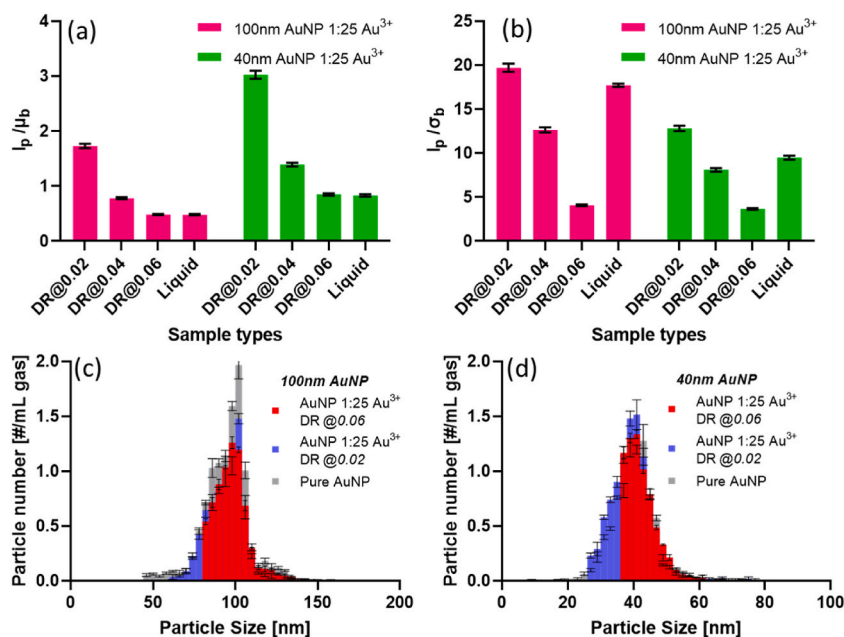
Fig. 6. The ratio of particle intensity (I_p) to average of ionic background intensity (μ_b) **(a)** and standard deviation of ionic background intensity (σ_b) **(b)** in each sample (AuNPs: Au^{3+} (1:25)). **(c)** Particle size distributions of 100 nm AuNPs and 100 nm AuNPs: Au^{3+} (1:25) at different RDD DR (nominally 0.02 and 0.06). **(d)** Particle size distributions of 40 nm AuNPs and 40 nm AuNPs: Au^{3+} (1:25) at different RDD DR (nominally 0.02 and 0.06).

included in the proposed method for size fractionation analysis. With the setup of Fig. S1, the size fractionation resolutions of DMA and CPMA were verified. The nominal size resolution (R_S) in CPMA is defined in **Equation S2**.

For DMA, the particle fractionation was based on the force balance between the drag force and electrostatic force of the charged particle (Tan et al., 2016). Therefore, only particles at specific sizes would be selected in DMA. As shown in Fig. 7a, the resolution for the DMA particle size selection was better in the smaller size range compared to the larger one. The peak in normalized fraction decreased from 0.24 for 40 nm particles to 0.19 for 100 nm particles. For each particle size selection, a second small peak could be found due to the double-charged particles at larger particle sizes selected at the DMA, which had the same electric mobility as the selected size particles (Hess et al., 2016; Hsieh, Lin, Hsiao, & Hou, 2022). When using CPMA for particle selection, the particle fractionation was based on the force balance between the centrifuge force between the two columns and the electrostatic force (Johnson et al., 2013). Therefore, the particle at a specific mass would be selected based on the rotating speed and the voltage applied in the CPMA (Equation (3)). When selecting R_s of 5 (Fig. 7b), the peak width got much wider than DMA. When selecting from 40 nm to 100 nm, the peak decreased from 0.050 to 0.018, which was only 9.5%–20.8% compared to those obtained by DMA. When R_s at 10 (Fig. 7c), the fractionation resolution was better, where the peak was around two times higher than the resolution of 5, indicating the double resolution level, but still around 17.0%–41.7% compared to those obtained by DMA. Similar to DMA, another peak at a larger size could be obtained due to the presence of double-charged particles. The main reason for a wider peak in CPMA compared to DMA was due to the width of the two electrodes in CPMA, where the particles of mass-to-charge ratios marginally higher and lower than the setpoint also passed through the classifier (Naseri, Johnson, Smallwood, & Olfert, 2023). In addition, compared to DMA, in both nominal resolutions, there was another particle peak at small sizes. This effect was more obvious when selecting larger particles (i.e. selecting 100 nm compared to 40 nm). This is because the CPMA rotated at a lower speed when selecting larger particles. Hence, small
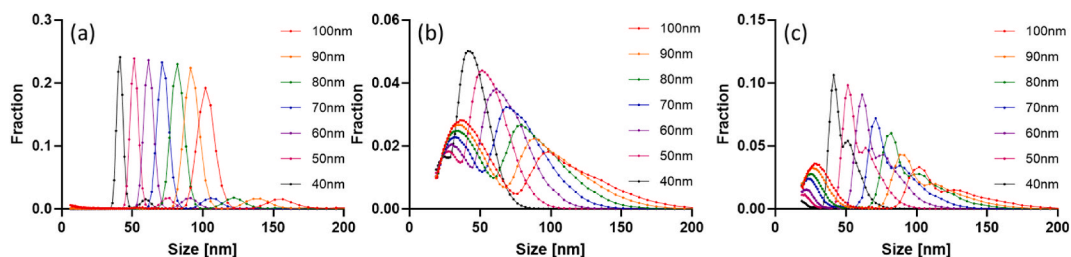

Fig. 7. Normalized NaCl particle size distribution when using DMA (a) and CPMA at different nominal size resolutions (R_s) of 5 (b) and 10 (c) for size fractionation of 40, 50, 60, 70, 80, 90, and 100 nm particles, respectively.

uncharged particles could also pass through the classifier (Naseri et al., 2023). Although CPMA could adjust the resolution level manually to reduce the amount of small uncharged particles and decrease the peak size, the resolution could not be increased because the number of AuNPs exiting the classifier needed to be adequate for spICP-MS characterization. Therefore, R_s of 5 and 10 were used in this project.

As can be seen in Fig. S7, when scanning from 80 nm to 120 nm in DMA, the ionic background decreased to 25 counts, indicating the contribution of Au^{3+} decreased after DMA fractionation (Fig. S10). While for CPMA using the same scanning program, the ionic signal decreased from 450 to 400 counts at the resolution of 5. When increasing the resolution to 10, the ionic background decreased from 375 to 368 counts (Fig. S10). Compared to the original ionic signal of 3088 counts (Fig. 4b), CPMA could reduce the ionic interference but was not as powerful as DMA. These results also refer to Fig. 7, where in CPMA small uncharged particles could still pass through the classifier when selecting large particles. In addition, in each case, some peaks with double intensity could be observed due to the double-charged particles or double events in spICP-MS. Therefore, an extra upper-limit threshold of $\mu_P+2\sigma_p$ was applied to remove the higher peaks based on the method described in a previous study (Tan et al., 2016). Then, the intensity data was transferred into size as it is shown in Fig. 8.

For both DMA and CPMA, the size and frequency of 100 nm AuNPs mixed with Au^{3+} (ratio 1:25) increased by increasing the scanned size up to 100 nm. From 100 nm to 120 nm, the size continued increasing but the frequency of particles decreased, indicating the presence of a few larger-sized AuNPs. The same experiment was carried out for 40 nm AuNPs mixed with Au^{3+} at a mass concentration ratio of 1:25 (Figs. S8 and S9). In this case, the scanning size range was set from 30 nm to 60 nm. The ionic background after DMA fractionation was decreased to 2 counts, which was much lower than the initial ionic intensity at around 140 counts (Fig. S10). For CPMA, when working at a nominal resolution of 5, the ionic background level decreased from 26 to 13 counts, and when using a resolution of 10 the ionic background level was always around 10 counts. Similar to the 100 nm AuNP mixture sample, the particle size and frequency increased from 30 nm to 40 nm. When scanning from 40 nm to 60 nm, still there were some particles but the frequency decreased.

Although the initial particle number concentration of 40 nm AuNPs in the liquid suspension was the same as in the 100 nm AuNPs suspension, the number of 40 nm AuNPs detected in spICP-MS was much less. For DMA, the particle number of 40 nm AuNPs detected in spICP-MS was 37% with respect to the number obtained of 100 nm AuNPs. For CPMA, the number of 40 nm AuNPs was 72% and 53% with respect to the number obtained for 100 nm AuNPs at the R_s of 5 and 10 respectively. The difference in the behavior with 100 nm and 40 nm AuNPs for DMA could be explained by the size of the Au^{3+} particles formed during the drying step. As it is shown in
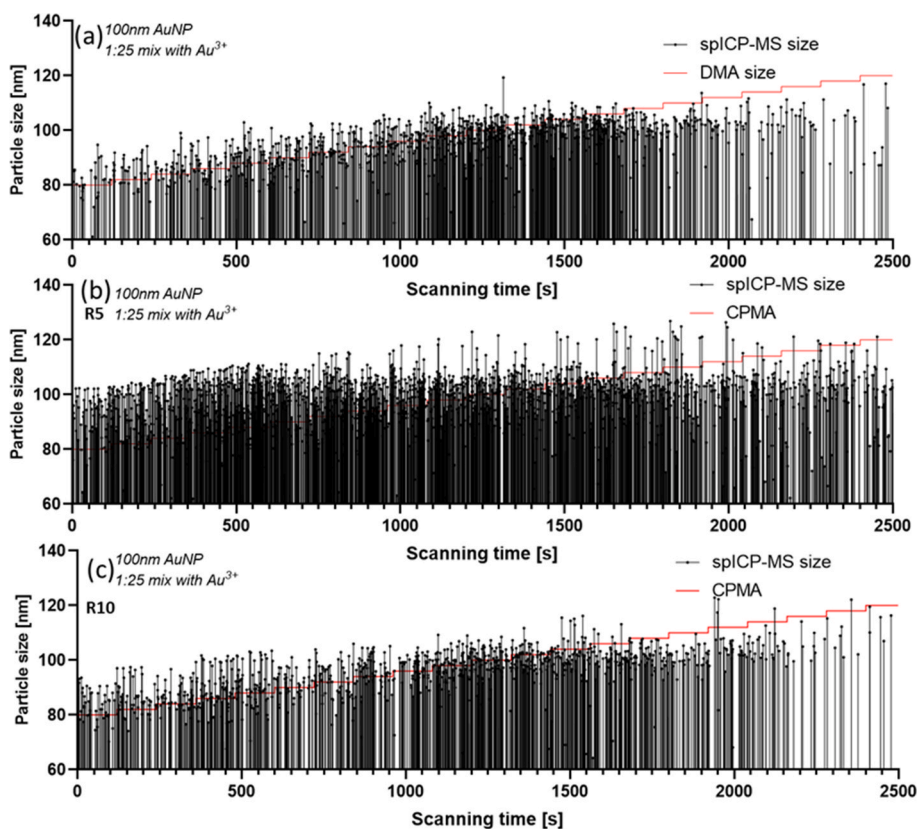

Fig. 8. AuNPs size from 100 nm AuNPs mixed with Au^{3+} (ratio 1:25) obtained after fractionation of DMA (a) or CPMA with the nominal resolution of 5 (b) and 10 (c) and analyzed by spICP-MS.

Fig. S11, the particle size distribution of pure AuNPs, pure Au^{3+} and mixed samples could be obtained directly from SMPS. For pure AuNPs, the particle size distributions were covered by the solvent background (sodium citrate), since the particle number of AuNP was much less than the amount of particles generated from sodium citrate. In both pure metal salts (Au^{3+}) and mixed samples (AuNPs/Au^{3+}), most of the Au^{3+} particles were around 40 nm, and fewer Au^{3+} particles were present around 100 nm in SMPS. For DMA, the separation is based on the particle size (Equation (2)). Therefore, it is much easier to separate the 100 nm AuNPs from the ionic interference in DMA compared to 40 nm AuNPs, since most of Au^{3+} is around 40 nm. However, for CPMA, the separation is based on particle mass (Equation (3)). With the same size, the mass of AuNP is much larger than Au^{3+} due to the higher density of AuNPs. Therefore, compared to DMA, more 40 nm AuNPs could be separated from the ionic interference by CPMA.

When comparing the size information from fractionation and spICP-MS, two-dimension particle size distribution heat maps could be obtained for both 40 and 100 nm AuNPs mixed with Au^{3+} (ratio 1:25) samples (Fig. 9). For the 100 nm AuNP mixture sample fractionated with DMA (Fig. 9a), most AuNPs were scattered around their nominal sizes (along the diagonal from left-bottom to right-up). This indicates the good selection in DMA and good characterization in spICP-MS for 100 nm AuNPs. For CPMA, when selecting R_s of 5 (Fig. 9b), more particles could be selected and then analyzed by spICP-MS. However, the resolution was not as good as the DMA fractionation (Fig. 9a). By increasing the R_s from 5 to 10, a better resolution similar to DMA could be achieved (Fig. 9c), but fewer particles were found. This effect indicated that for CPMA it was always a choice between ionic reduction or the number of particles counted when doing fractionation. For the 40 nm AuNP mixture sample (Fig. 9d–f), the separation was worse than the 100 nm AuNP mixture sample with both tested fractionation techniques, due to the higher diffusion loss and lower charge efficiency of smaller particles (W. Yang, Zhu, Wang, & Liu, 2019). In addition, as can be observed in Fig. S12, after fractionation of DMA or CPMA, is possible to obtain particle size distributions similar to the ones determined for pure AuNPs by using RDD-spICP-MS. This indicates that both separation technologies have the ability to reduce ionic interference for metallic particle characterization.

3.4. Comparison of separation based on online dilution and fractionation methods

To compare the effectiveness of the proposed technologies for separating the NPs signals from the ionic background, a comparison analysis was performed with the RDD, the DMA, and the CPMA. As can be observed in Fig. 10a and b, both fractionation techniques (DMA and CPMA) and online dilution (RDD) could decrease the limit of detection. For a 3 times online dilution of 100 nm AuNPs mixed with 25 times concentrated Au^{3+} by RDD (nominal DR decreased from 0.06 to 0.02), the LOD_{size} decreased from 78 nm to 61 nm. When
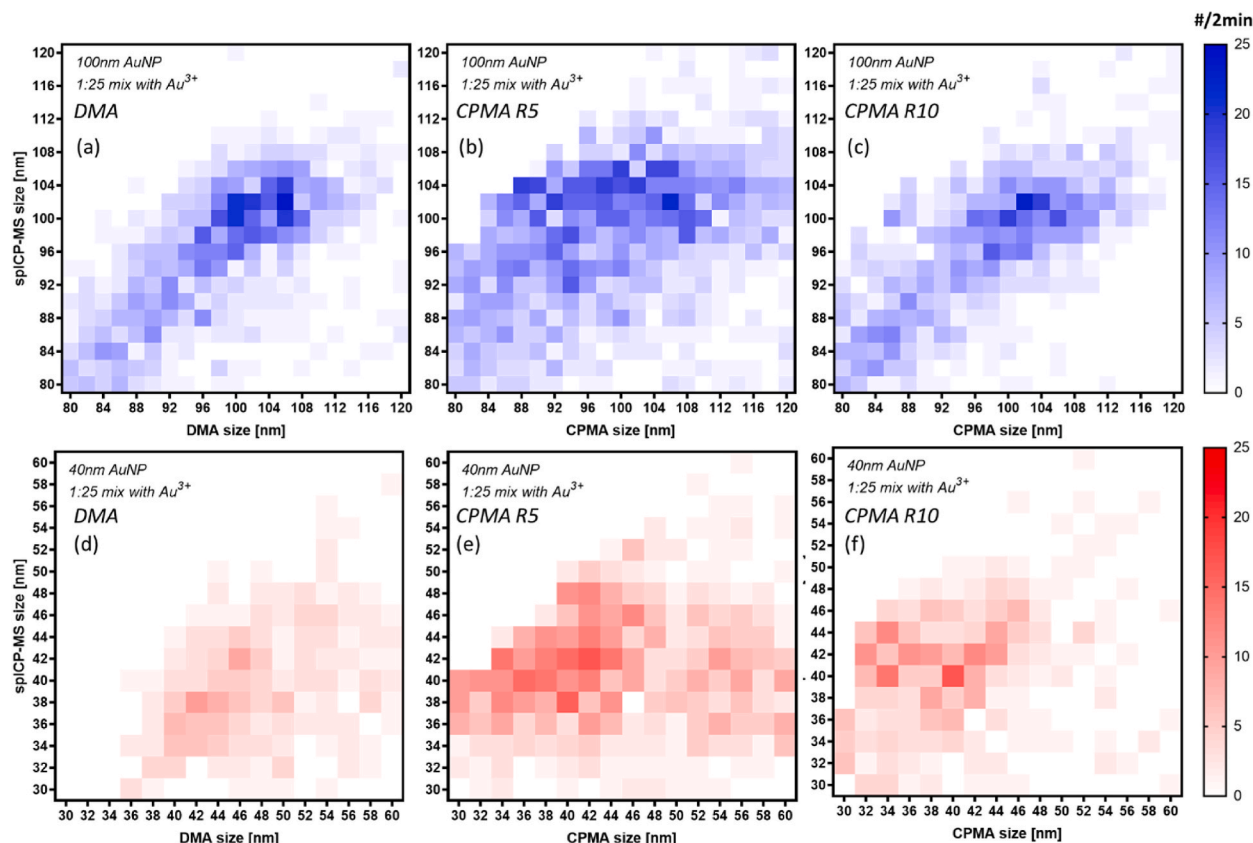

Fig. 9. Heat maps of the two-dimension particle size distribution of 100 nm AuNPs (a–c) and 40 nm AuNPs (d–f) mixed with Au^{3+} (ratio of 1:25) obtained after fractionation of DMA (a, and d, x-axis) or CPMA (b, c, e, and f, x-axis) and analyzed by spICP-MS (y-axis).
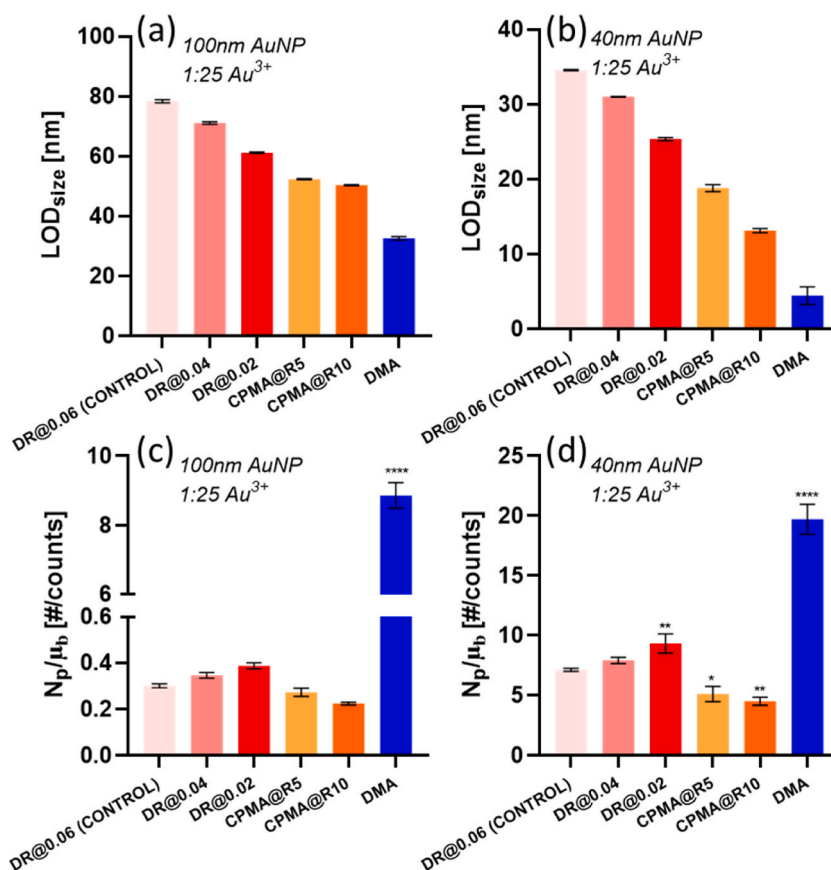
Fig. 10. LOD$_{size}$ (a, b) and the ratio between particle number and average ionic background intensity (Np/μ_b, c, d) of 100 nm and 40 nm AuNPs mixed with Au^{3+} at 1:25 mass ratio. ANOVA tests were done when comparing different separation methods with respect to the control sample (****P < 0.0001, **P < 0.01, *P < 0.05).

CPMA and DMA were used, they could be reduced to 50 nm and 33 nm respectively. However, for signal separation, we should not only consider how much ionic interference was removed but also how many particles were lost. To better evaluate the effectiveness of the AuNPs and Au^{3+} signal separation, a separation factor was defined as the ratio of the number of particles to the average of ionic background intensity (Np/μ_b). In theory, this separation factor should be constant during the dilution process since N$_p$ and μ_b decrease proportionally at each RDD DR. However, as shown in Fig. 10c and d, for both 40 and 100 nm AuNPs mixed with Au^{3+} (ratio 1:25), the separation factor increased slightly with dilution (nominal DR decreased from 0.06 to 0.02). Compared to RDD dilution, the separation factors of CPMA at different resolutions were lower. This indicates, that the effect of size selection by CPMA is not as good as online dilution, which may be attributed to the passing of uncharged small Au^{3+} particles during the AuNPs fractionation counted as false positive events (Naseri et al., 2023). However, when working with DMA fractionation, it showed the separation improved 29.5 times for the 100 nm AuNP mixture and 2.8 times for the 40 nm AuNP mixture with Au^{3+} at the ratio of 1:25. To sum up, the ability of separation would be DMA > RDD > CPMA in the aerosol for online spICP-MS characterization of both 40 and 100 nm AuNPs in presence of ionic gold at a ratio of 1:25 (AuNPs:Au^{3+}). In real environmental aerosol samples, usually, the target particle sizes are unknown. In this case, online dilution of RDD could still be used as a general method. However, DMA and CPMA, are required to scan a broader size (or mass for CPMA) range to separate the particles present in the sample with an unknown size.

4. Conclusion

In this study, the effect of the presence of metal salts for nanoparticle characterization in the aerosol by spICP-MS was investigated. The aerosol contained metallic nanoparticles (AuNPs) and metal salts (Au^{3+}) which were generated from a concentric nebulizer combined with a silica dryer. To better characterize the AuNPs, different separation technologies were evaluated for ionic background reduction. With the same nebulizer introduction system, AuNP signals present individual peaks in spICP-MS in both liquid and aerosol modes. However, different behavior of Au^{3+} in liquid and aerosol modes could be found. In liquid mode, Au^{3+} would form droplets with homogenous concentrations and reach the ICP detector continuously as a stable baseline. In contrast, in aerosol mode, the Au^{3+} would form different sized salt particles after the dryer. These salt particles would reach ICP detector more heterogeneously compared to wet droplets containing Au^{3+}, causing a much larger variation in the ionic background.

For separating the nanoparticle signal from the ionic background, three technologies including RDD, DMA, and CPMA were evaluated. RDD could effectively reduce the ionic background for better AuNPs characterization by diluting online the aerosol (nominal DR decreased from 0.06 to 0.02). When working with online fractionation by CPMA or DMA, the LOD_{size} decreased, improving AuNPs characterization. To compare these three separation methods quantitatively, a separation factor was defined as the ratio between the particle number and the average of ionic background intensity (Np/μ_b). It was shown that the performance order of the three techniques to reduce Au^{3+} for AuNPs characterization by spICP-MS in aerosol was DMA > RDD > CPMA. This study showed the capability for the reduction of ionic interference in the aerosol by coupling RDD, DMA, or CPMA to spICP-MS for characterizing metallic nanoparticles.

CRediT authorship contribution statement

Tianyu Cen: Conceptualization, Data curation, Formal analysis, Investigation, Methodology, Validation, Visualization, Writing – original draft, Writing – review & editing. **Yi-Bo Zhao:** Formal analysis, Investigation, Resources, Writing – review & editing. **Andrea Testino:** Project administration, Supervision, Writing – review & editing. **Jing Wang:** Formal analysis, Validation, Writing – review & editing. **Laura Torrent:** Conceptualization, Formal analysis, Investigation, Methodology, Supervision, Validation, Visualization, Writing – review & editing. **Christian Ludwig:** Conceptualization, Funding acquisition, Project administration, Resources, Supervision, Writing – review & editing.

Declaration of competing interest

The authors declare that they have no known competing financial interests or personal relationships that could have appeared to influence the work reported in this paper.

Data availability

Data will be made available on request.

Acknowledgments

Appendix A. Supplementary data

Supplementary data to this article can be found online at https://doi.org/10.1016/j.jaerosci.2023.106317.

References

Alves, C., Vicente, A., Nunes, T., Gonçalves, C., Fernandes, A. P., Mirante, F., et al. (2011). Summer 2009 wildfires in Portugal: Emission of trace gases and aerosol composition. *Atmospheric Environment, 45*(3), 641–649. https://doi.org/10.1016/j.atmosenv.2010.10.031

Bierwirth, M., Olszok, V., Wollmann, A., & Weber, A. P. (2022). A new coupling setup of DMA, CPC and sp-ICP-MS with increased versatility. *Journal of Aerosol Science, 163*, 105983. https://doi.org/10.1016/j.jaerosci.2022.105983

Bolea, E., Jimenez, M. S., Perez-Arantegui, J., Vidal, J. C., Bakir, M., Ben-Jeddou, K., et al. (2021). Analytical applications of single particle inductively coupled plasma mass spectrometry: A comprehensive and critical review. *Analytical Methods, 13*, 2742–2795. https://doi.org/10.1039/d1ay00761k

Cen, T., Torrent, L., Testino, A., & Ludwig, C. (2023a). Rotating disk diluter hyphenated with single particle ICP-MS as an online dilution and sampling platform for metallic nanoparticles characterization in ambient aerosol. *Journal of Aerosol Science, 175*, Article 106283. https://doi.org/10.1016/j.jaerosci.2023.106283

Cen, T., Torrent, L., Testino, A., & Ludwig, C. (2023b). Rotating disk diluter hyphenated with single particle ICP-MS as an online dilution and sampling platform for metallic nanoparticles characterization in ambient aerosol. *Journal of Aerosol Science, 175*, Article 106283. https://doi.org/10.1016/j.jaerosci.2023.106283. August 2023.

Cornelis, G., & Hassellöv, M. (2013). A signal deconvolution method to discriminate smaller nanoparticles in single particle ICP-MS. *Journal of Analytical Atomic Spectrometry, 29*(1), 134–144. https://doi.org/10.1039/C3JA50160D

Csavina, J., Field, J., Taylor, M. P., Gao, S., Landázuri, A., Betterton, E. A., et al. (2012). A review on the importance of metals and metalloids in atmospheric dust and aerosol from mining operations. *Science of the Total Environment, 433*, 58–73. https://doi.org/10.1016/j.scitotenv.2012.06.013

Edmonds, M., Mason, E., & Hogg, O. (2022). Volcanic outgassing of volatile trace metals. *Annual Review of Earth and Planetary Sciences, 50*, 79–98. https://doi.org/10.1146/annurev-earth-070921-062047

Egorova, K. S., & Ananikov, V. P. (2017). Toxicity of metal compounds: Knowledge and myths. *Organometallics, 36*(21), 4071–4090. https://doi.org/10.1021/acs.organomet.7b00605

Foppiano, D., Tarik, M., Gubler Müller, E., & Ludwig, C. (2018a). Combustion generated nanomaterials: Online characterization: Via an ICP-MS based technique. Part II: Resolving power for heterogeneous matrices. *Journal of Analytical Atomic Spectrometry, 33*(9), 1500–1505. https://doi.org/10.1039/c8ja00067k

Foppiano, D., Tarik, M., Müller Gubler, E., & Ludwig, C. (2018b). Emissions of secondary formed ZnO nano-objects from the combustion of impregnated wood. An online size-resolved elemental investigation. *Environmental Science and Technology, 52*(2), 895–903. https://doi.org/10.1021/acs.est.7b03584

Furger, M., Minguillón, M. C., Yadav, V., Slowik, J. G., Hüglin, C., Fröhlich, R., et al. (2017). Elemental composition of ambient aerosols measured with high temporal resolution using an online XRF spectrometer. *Atmospheric Measurement Techniques, 10*(6), 2061–2076. https://doi.org/10.5194/amt-10-2061-2017

Furger, M., Rai, P., Slowik, J. G., Cao, J., Visser, S., Baltensperger, U., et al. (2020). Automated alternating sampling of PM10 and PM2. 5 with an online XRF spectrometer. *Atmospheric Environment, X, 5*, 100065. https://doi.org/10.1016/j.aeaoa.2020.100065

Giannoukos, S., Lee, C. P., Tarik, M., Ludwig, C., Biollaz, S., Lamkaddam, H., et al. (2020). Real-time detection of aerosol metals using online extractive electrospray ionization mass spectrometry. *Analytical Chemistry, 92*, 1316–1325. https://doi.org/10.1021/acs.analchem.9b04480

Giannoukos, S., Tarik, M., Ludwig, C., Biollaz, S., Slowik, J., Baltensperger, U., et al. (2021). Detection of trace metals in biogas using extractive electrospray ionization high-resolution mass spectrometry. *Renewable Energy, 169*, 780–787. https://doi.org/10.1016/j.renene.2021.01.047

Gundlach-Graham, A., & Lancaster, R. (2022). Mass-dependent critical value expressions for particle finding in single-particle ICP-tofms. *Analytical Chemistry, 95(13)*, 5618-5626. https://doi.org/10.1021/acs.analchem.2c05243

Hadioui, M., Merdzan, V., & Wilkinson, K. J. (2015). Detection and characterization of ZnO nanoparticles in surface and waste waters using single particle ICPMS. *Environmental Science and Technology, 49*(10), 6141–6148. https://doi.org/10.1021/acs.est.5b00681

Hadioui, M., Peyrot, C., & Wilkinson, K. J. (2014). Improvements to single particle ICPMS by the online coupling of ion exchange resins. *Analytical Chemistry, 86*(10), 4668–4674. https://doi.org/10.1021/ac5004932

Haghani, A., Johnson, R., Safi, N., Zhang, H., Thorwald, M., Mousavi, A., et al. (2020). Toxicity of urban air pollution particulate matter in developing and adult mouse brain: Comparison of total and filter-eluted nanoparticles. *Environment International, 136*, Article 105510. https://doi.org/10.1016/j.envint.2020.105510

Hess, A., Tarik, M., Losert, S., Ilari, G., & Ludwig, C. (2016). Measuring air borne nanoparticles for characterizing hyphenated RDD-SMPS-ICPMS instrumentation. *Journal of Aerosol Science, 92*, 130–141. https://doi.org/10.1016/j.jaerosci.2015.10.007

Hetzer, B., Burcza, A., Gräf, V., Walz, E., & Greiner, R. (2017). Online-coupling of AF4 and single particle-ICP-MS as an analytical approach for the selective detection of nanosilver release from model food packaging films into food simulants. *Food Control, 80*, 113–124. https://doi.org/10.1016/j.foodcont.2017.04.040

Hsieh, Y.-C., Lin, Y.-P., Hsiao, T.-C., & Hou, W.-C. (2022). A two-dimensional nanoparticle characterization method combining differential mobility analyzer and single-particle inductively coupled plasma-mass spectrometry with an atomizer-enabled sample introduction (ATM-DMA-spICP-MS): Toward the analysis of hetero. *The Science of the Total Environment, 838*, 156444. https://doi.org/10.1016/j.scitotenv.2022.156444

Jahn, L. G., Jahl, L. G., Bland, G. D., Bowers, B. B., Monroe, L. W., & Sullivan, R. C. (2021). Metallic and crustal elements in biomass-burning aerosol and ash: Prevalence, significance, and similarity to soil particles. *ACS Earth and Space Chemistry, 5*(1), 136–148. https://doi.org/10.1021/acsearthspacechem.0c00191

Jiang, H., Wang, Y., Tan, Z., Hu, L., Shi, J., Liu, G., et al. (2023). Dissolved metal ion removal by online hollow fiber ultrafiltration for enhanced size characterization of metal-containing nanoparticles with single-particle ICP-MS. *Journal of Environmental Sciences, 126*, 494–505. https://doi.org/10.1016/j.jes.2022.05.034

Johnson, T. J., Symonds, J. P. R., & Olfert, J. S. (2013). Mass-mobility measurements using a centrifugal particle mass analyzer and differential mobility spectrometer. *Aerosol Science and Technology, 47*(11), 1215–1225. https://doi.org/10.1080/02786826.2013.830692

Laborda, F., Gimenez-Ingalaturre, A. C., Bolea, E., & Castillo, J. R. (2020). *About detectability and limits of detection in single particle inductively coupled plasma mass spectrometry*. Spectrochimica Acta - Part B Atomic Spectroscopy, 169, 105883. https://doi.org/10.1016/j.sab.2020.105883

López-Mayan, J., Barciela-Alonso, M. C., Domínguez-González, M. R., Peña-Vázquez, E., & Bermejo-Barrera, P. (2020). Cloud point extraction and ICP-MS for titanium speciation in water samples. *Microchemical Journal, 152*, Article 104264. https://doi.org/10.1016/j.microc.2019.104264

Luo, L., Yang, Y., Li, H., Ding, R., Wang, Q., & Yang, Z. (2018). Size characterization of silver nanoparticles after separation from silver ions in environmental water using magnetic reduced graphene oxide. *Science of the Total Environment, 612*, 1215–1222. https://doi.org/10.1016/j.scitotenv.2017.09.024

Mahowald, N. M., Hamilton, D. S., Mackey, K. R. M., Moore, J. K., Baker, A. R., Scanza, R. A., et al. (2018). Aerosol trace metal leaching and impacts on marine microorganisms. *Nature Communications, 9*(1), 2614. https://doi.org/10.1038/s41467-018-04970-7

Mason, E., Wieser, P. E., Liu, E. J., Edmonds, M., Ilyinskaya, E., Whitty, R. C. W., et al. (2021). Volatile metal emissions from volcanic degassing and lava–seawater interactions at Kīlauea Volcano, Hawai'i. *Communications Earth & Environment, 2*(1), 79. https://doi.org/10.1038/s43247-021-00145-3

Meili-Borovinskaya, O., Meier, F., Drexel, R., Baalousha, M., Flamigni, L., Hegetschweiler, A., et al. (2021). Analysis of complex particle mixtures by asymmetrical flow field-flow fractionation coupled to inductively coupled plasma time-of-flight mass spectrometry. *Journal of Chromatography A, 1641*, Article 461981. https://doi.org/10.1016/j.chroma.2021.461981

Mettakoonpitak, J., Volckens, J., & Henry, C. S. (2019). Janus electrochemical paper-based analytical devices for metals detection in aerosol samples. *Analytical Chemistry, 92*(1), 1439–1446. https://doi.org/10.1021/acs.analchem.9b04632

Moreno, T., Querol, X., Alastuey, A., Amato, F., Pey, J., Pandolfi, M., et al. (2010). Effect of fireworks events on urban background trace metal aerosol concentrations: Is the cocktail worth the show? *Journal of Hazardous Materials, 183*(1–3), 945–949. https://doi.org/10.1016/j.jhazmat.2010.07.082

Moreno, T., Querol, X., Alastuey, A., Reche, C., Cusack, M., Amato, F., et al. (2011). Variations in time and space of trace metal aerosol concentrations in urban areas and their surroundings. *Atmospheric Chemistry and Physics, 11*(17), 9415–9430. https://doi.org/10.5194/acp-11-9415-201

Mozhayeva, D., & Engelhard, C. (2020). A critical review of single particle inductively coupled plasma mass spectrometry – a step towards an ideal method for nanomaterial characterization. *Journal of Analytical Atomic Spectrometry, 35*, 1740-1783. https://doi.org/10.1039/c9ja00206e

Myojo, T., Takaya, M., & Ono-Ogasawara, M. (2002). DMA as a gas converter from aerosol to "Argonsol" for real-time chemical analysis using ICP-MS. *Aerosol Science and Technology, 36*(1), 76–83. https://doi.org/10.1080/027868202753339096

Naseri, A., Johnson, T. J., Smallwood, G., & Olfert, J. S. (2023). Measurement of the centrifugal particle mass analyzer transfer function. *Aerosol Science and Technology, 57*(10), 963–980. https://doi.org/10.1080/02786826.2023.2228378

Ohata, M., & Nishiguchi, K. (2017). Direct analysis of gaseous mercury in ambient air by gas to particle conversion-gas exchange ICPMS. *Journal of Analytical Atomic Spectrometry, 32*(4), 717–722. https://doi.org/10.1039/c6ja00292g

Ohata, M., Sakurai, H., Nishiguchi, K., Utani, K., & Günther, D. (2015). Direct analysis of ultra-trace semiconductor gas by inductively coupled plasma mass spectrometry coupled with gas to particle conversion-gas exchange technique. *Analytica Chimica Acta, 891*, 73–78. https://doi.org/10.1016/j.aca.2015.06.048

Olesik, J. W., & Gray, P. J. (2012). Considerations for measurement of individual nanoparticles or microparticles by ICP-MS: Determination of the number of particles and the analyte mass in each particle. *Journal of Analytical Atomic Spectrometry, 27*(7), 1143–1155. https://doi.org/10.1039/c2ja30073g

Olfert, J. S., Reavell, K. S. J., Rushton, M. G., & Collings, N. (2006). The experimental transfer function of the Couette centrifugal particle mass analyzer. *Journal of Aerosol Science, 37*(12), 1840–1852. https://doi.org/10.1016/j.jaerosci.2006.07.007

Pace, H. E., Rogers, N. J., Jarolimek, C., Coleman, V. A., Higgins, C. P., & Ranville, J. F. (2011). Determining transport efficiency for the purpose of counting and sizing nanoparticles via single particle inductively coupled plasma mass spectrometry. *Analytical Chemistry, 83*(24), 9361–9369. https://doi.org/10.1021/ac201952t

Pergantis, S. A., Jones-Lepp, T. L., & Heithmar, E. M. (2012). Hydrodynamic chromatography online with single particle-inductively coupled plasma mass spectrometry for ultratrace detection of metal-containing nanoparticles. *Analytical Chemistry, 84*(15), 6454–6462. https://doi.org/10.1021/ac300302j

Schwertfeger, D. M., Velicogna, J. R., Jesmer, A. H., Scroggins, R. P., & Princz, J. I. (2016). Single particle-inductively coupled plasma mass spectroscopy analysis of metallic nanoparticles in environmental samples with large dissolved analyte fractions. *Analytical Chemistry, 88*(20), 9908–9914. https://doi.org/10.1021/acs.analchem.6b02716

Strenge, I., & Engelhard, C. (2016). Capabilities of fast data acquisition with microsecond time resolution in inductively coupled plasma mass spectrometry and identification of signal artifacts from millisecond dwell times during detection of single gold nanoparticles. *Journal of Analytical Atomic Spectrometry, 31*(1), 135–144. https://doi.org/10.1039/C5JA00177C

Tan, J., Liu, J., Li, M., El Hadri, H., Hackley, V. A., & Zachariah, M. R. (2016). Electrospray-differential mobility hyphenated with single particle inductively coupled plasma mass spectrometry for characterization of nanoparticles and their aggregates. *Analytical Chemistry, 88*(17), 8548–8555. https://doi.org/10.1021/acs.analchem.6b01544

Tan, J., Yang, Y., El Hadri, H., Li, M., Hackley, V. A., & Zachariah, M. R. (2019). Fast quantification of nanorod geometry by DMA-spICP-MS. *The Analyst, 144*(7), 2275–2283. https://doi.org/10.1039/c8an02250j

Tarik, M., Foppiano, D., Hess, A., & Ludwig, C. (2017). A practical guide on coupling a scanning mobility sizer and inductively coupled plasma mass spectrometer (SMPS-ICPMS). *Journal of Visualized Experiments, 2017*(125), 1–9. https://doi.org/10.3791/55487

Torregrosa, D., Grindlay, G., Mora, J., & Gras, L. (2023). Unraveling the role of aerosol transport on nanomaterial characterization by means single particle inductively coupled plasma mass spectrometry. *Journal of Analytical Atomic Spectrometry, 38*, 1874–1884. https://doi.org/10.1039/D3JA00134B

Torrent, L., Laborda, F., Marguí, E., Hidalgo, M., & Iglesias, M. (2019). Combination of cloud point extraction with single particle inductively coupled plasma mass spectrometry to characterize silver nanoparticles in soil leachates. *Analytical and Bioanalytical Chemistry, 411*(20), 5317–5329. https://doi.org/10.1007/s00216-019-01914-y

Wimmer, A., Urstoeger, A., Hinke, T., Aust, M., Altmann, P. J., & Schuster, M. (2021). Separating dissolved silver from nanoparticulate silver is the key: Improved cloud-point-extraction hyphenated to single particle ICP-MS for comprehensive analysis of silver-based nanoparticles in real environmental samples down to single-digit nm particl. *Analytica Chimica Acta, 1150*, Article 238198. https://doi.org/10.1016/j.aca.2021.01.001

Yang, J., Ma, L., He, X., Au, W. C., Miao, Y., Wang, W.-X., et al. (2023). Measurement report: Abundance and fractional solubilities of aerosol metals in urban Hong Kong–insights into factors that control aerosol metal dissolution in an urban site in South China. *Atmospheric Chemistry and Physics, 23*(2), 1403–1419. https://doi.org/10.5194/acp-23-1403-2023

Yang, W., Zhu, R., Wang, L., & Liu, B. (2019). Charging efficiency of nanoparticles in needle-to-plate chargers with micro discharge gaps. *Journal of Nanoparticle Research, 21*, 1–10. https://doi.org/10.1007/s11051-019-4572-8

Zauscher, M. D., Wang, Y., Moore, M. J. K., Gaston, C. J., & Prather, K. A. (2013). Air quality impact and physicochemical aging of biomass burning aerosols during the 2007 San Diego wildfires. *Environmental Science & Technology, 47*(14), 7633–7643. https://doi.org/10.1021/es4004137

Zhao, D., Aravindakshan, A., Hilpert, M., Olmedo, P., Rule, A. M., Navas-Acien, A., et al. (2020). Metal/metalloid levels in electronic cigarette liquids, aerosols, and human biosamples: A systematic review. *Environmental Health Perspectives, 128*(3). https://doi.org/10.1289/EHP5686

Zhao, Y.-B., Cen, T., Jiang, F., He, W., Zhang, X., Feng, X., et al. (2023). Aerosol-into-liquid capture and detection of atmospheric soluble metals across the gas–liquid interface using Janus-membrane electrodes. *Proceedings of the National Academy of Sciences, 120*(10), Article e2219388120. https://doi.org/10.1073/pnas.2219388120

Zhao, Y. B., Tang, J., Cen, T., Qiu, G., He, W., Jiang, F., et al. (2022). Integrated aerodynamic/electrochemical microsystem for collection and detection of nanogram-level airborne bioaccessible metals. *Sensors and Actuators B: Chemical, 351*, Article 130903. https://doi.org/10.1016/j.snb.2021.130903